


Cite this: *RSC Adv.*, 2017, 7, 55269

# Metallic 1T-TiS<sub>2</sub> nanodots anchored on a 2D graphitic C<sub>3</sub>N<sub>4</sub> nanosheet nanostructure with high electron transfer capability for enhanced photocatalytic performance

Yang Liu,<sup>†ab</sup> Xiaojie She,<sup>†c</sup> Xiaoni Zhang,<sup>c</sup> Chenglu Liang,<sup>ab</sup> Jingjie Wu,<sup>b</sup> Peng Yu,<sup>a</sup> Yusuke Nakanishi,<sup>b</sup> Banghu Xie,<sup>a</sup> Hui Xu,<sup>id</sup>\*<sup>c</sup> Pulickel M. Ajayan<sup>b</sup> and Wei Yang<sup>id</sup>\*<sup>a</sup>

Photocatalysis is one of the most promising technologies for solar energy conversion. With the development of photocatalysis technology, the creation of low-dimensional structure photocatalysts with improved properties becomes more and more important. Metallic 1T-TiS<sub>2</sub> nanodots with a low-dimensional structure were introduced into environmentally friendly two-dimensional g-C<sub>3</sub>N<sub>4</sub> (2D-C<sub>3</sub>N<sub>4</sub>) nanosheets by a solvothermal method. It was found that the ultrathin TiS<sub>2</sub> nanodots were uniformly anchored on the surface of the 2D-C<sub>3</sub>N<sub>4</sub>. The effective suppression of electron-hole recombination was realized due to the addition of the intrinsic metallic property of 1T-TiS<sub>2</sub> in the prepared nanocomposite. The 5 wt% TiS<sub>2</sub>/2D-C<sub>3</sub>N<sub>4</sub> nanocomposite exhibited the best photocatalytic performance and the degradation rate towards RhB was ca. 95% in 70 min, which showed an improvement of ca. 30% in comparison with 2D-C<sub>3</sub>N<sub>4</sub>. The results indicate that the obtained TiS<sub>2</sub>/2D-C<sub>3</sub>N<sub>4</sub> nanocomposite is a promising photocatalyst for practical applications.

Received 30th September 2017  
Accepted 27th November 2017

DOI: 10.1039/c7ra10826e

rsc.li/rsc-advances

## Introduction

With the increasing scarcity of conventional energy resources and the deterioration of the environment, the development and utilization of renewable energy becomes more and more important.<sup>1</sup> Solar power can be converted by photocatalysts into chemical energy to degrade pollutants, which has attracted a lot of attention in the past decades.<sup>2</sup> Numerous researchers have devoted themselves to creating efficient photocatalysts to take full advantage of the redox ability of photogenerated carriers. TiO<sub>2</sub> was reported to be used for hydrogen generation *via* water splitting under ultraviolet light.<sup>3–6</sup> Nevertheless, the challenges of photocatalytic degradation mainly lie in the following two points: (1) the wide light absorption range and (2) the efficient separation of photogenerated electrons and holes.<sup>7,8</sup>

In recent years, researchers have found the dimension reduction of the photocatalysts can shorten the diffusion length of photogenerated carriers.<sup>9–16</sup> Moreover, the introduction of conducting materials has been found to be able to suppress

recombination of photogenerated electron (e)–hole (h) pairs of semiconductors, such as some noble metals (Ag, Au and Pt).<sup>17–22</sup> Platinum (Pt) with the lowest Fermi level is the most effective acceptor of photogenerated electrons for the photocatalytic reaction.<sup>23</sup> However, its high material cost makes it uncompetitive for practical applications. Thus, the development of the substitute materials (noble metal-free) of the noble metals is very necessary, but still challenging to date.

Layered transition metal dichalcogenides (TMDs) such as MoS<sub>2</sub>, WSe<sub>2</sub>, TaS<sub>2</sub> *etc.*, have received much attention owing to their excellent catalytic activity and low cost compared to noble metals.<sup>24–30</sup> As a prototype of TMDs, 1T-TiS<sub>2</sub> is composed of metal Ti layer sandwiched between two S layers forming edge-sharing TiS<sub>6</sub> octahedra with strong covalent forces.<sup>3</sup> The adjacent S–Ti–S layers are coupled to each other by weak van der Waals interactions, providing the practical feasibility for exfoliating the bulk TiS<sub>2</sub> to ultrathin two dimensional TiS<sub>2</sub> nanosheets.<sup>31,32</sup> In addition, 1T-TiS<sub>2</sub> is a semimetal with excellent in-plane conductivities.<sup>33</sup> It is noticeable that conductive 1T-TiS<sub>2</sub> can replace the noble metals to be used as the acceptor of the photogenerated electrons and improve the separation efficiency of the photoexcited carriers of semiconductors.

Graphitic carbon nitride (g-C<sub>3</sub>N<sub>4</sub>), a polymeric semiconductor with a low band gap of ~2.7 eV, has an appropriate band structure for photocatalysis.<sup>34</sup> Two dimensional C<sub>3</sub>N<sub>4</sub> (2D-C<sub>3</sub>N<sub>4</sub>) can be prepared according to our previous report.<sup>35–37</sup> The two dimensional structure of g-C<sub>3</sub>N<sub>4</sub> can contribute to the

<sup>a</sup>College of Polymer Science and Engineering, Sichuan University, State Key Laboratory of Polymer Materials Engineering, Chengdu 610065, Sichuan, China. E-mail: weiyang@scu.edu.cn

<sup>b</sup>Department of Materials Science and NanoEngineering, Rice University, 6100 Main Street, Houston, Texas 77005, USA

<sup>c</sup>Institute for Energy Research, Jiangsu University, Zhenjiang, 212013, P. R. China. E-mail: xh@ujs.edu.cn

<sup>†</sup> Authors contributed equally to this work.



separation of photogenerated e<sup>−</sup>–h<sup>+</sup> pairs and then the carriers could handily transfer to the surface to suppress the recombination.<sup>38–43</sup> However, the separation efficiency of the photoexcited carriers of 2D-C<sub>3</sub>N<sub>4</sub> are still unsatisfactory in the absence of noble metals. To further improve the photocatalytic activity of 2D-C<sub>3</sub>N<sub>4</sub>, the introduction of some conductive materials is an effective method.

Herein, the exfoliated ultrathin TiS<sub>2</sub> nanodots were introduced into 2D-C<sub>3</sub>N<sub>4</sub>. Anchoring metallic TiS<sub>2</sub> nanodots on 2D-C<sub>3</sub>N<sub>4</sub> nanosheets *via* solvothermal method facilitated the fast transfer of the photogenerated carriers. The high photocatalytic performance of the nanocomposite resulted from the effective suppression of the e<sup>−</sup>–h<sup>+</sup> recombination was tested by degrading Rhodamine B (RhB). In the nanocomposites, uniformly distributed TiS<sub>2</sub> nanodots on surface of 2D-C<sub>3</sub>N<sub>4</sub> nanosheets did serve as the acceptor of the photogenerated electrons. Additionally, the photocatalytic mechanism was also studied in detail by electron spin resonance (ESR).

## Experimental

### 1. Synthesis of ultrathin TiS<sub>2</sub> nanodots

Ultrathin TiS<sub>2</sub> nanodots were prepared *via* liquid phase exfoliation in a co-solvent (acetonitrile/IPA = 19 : 1, by volume). Specifically, 900 mg 1T-TiS<sub>2</sub> powder (Sigma-Aldrich) was dispersed in 300 ml co-solvent and the solution was sonicated in an ultrasonic bath at 25 °C for 4 h. Then the mixture was centrifuged at 6000 rpm for 30 min to remove any unexfoliated bulk TiS<sub>2</sub>. The supernatant was further probe sonicated for another 4 h followed by centrifugation at 10 000 rpm for 30 min. The freeze-dried supernatant was named as TiS<sub>2</sub> nanodots.

### 2. Synthesis of ultrathin g-C<sub>3</sub>N<sub>4</sub> nanosheets

Ultrathin g-C<sub>3</sub>N<sub>4</sub> was synthesized as below. 2 g melamine were calcined at 550 °C for 4 h with 2 °C min<sup>−1</sup> heating rate in the muffle furnace. The obtained sample was bulk g-C<sub>3</sub>N<sub>4</sub>. Then 400 mg bulk g-C<sub>3</sub>N<sub>4</sub> was ground and heated at 550 °C for ~30 min in the muffle furnace. After that, the obtained samples were heated at 550 °C for another ~30 min in the muffle furnace. Finally, the obtained ultrathin g-C<sub>3</sub>N<sub>4</sub> were white.

### 3. Synthesis of TiS<sub>2</sub>/2D-C<sub>3</sub>N<sub>4</sub> nanocomposites

The TiS<sub>2</sub>/2D-C<sub>3</sub>N<sub>4</sub> nanocomposite was prepared by solvothermal method in benzyl alcohol. An appropriate amount of ultrathin TiS<sub>2</sub> nanodots and 70 mg 2D-C<sub>3</sub>N<sub>4</sub> was dispersed in benzyl alcohol and sonicated for 20 min, respectively. Then a certain concentration of TiS<sub>2</sub> nanodots was mixed with pure 2D-C<sub>3</sub>N<sub>4</sub> and stirred for 2 h. After sonicating the mixture again for 20 min, the suspension was transferred to a stainless-steel autoclave and heated for 4 h at 140 °C. After natural cooling, the solution was washed by ethanol and water twice respectively. The washed powder was then freeze dried and used as catalyst. The TiS<sub>2</sub>/2D-C<sub>3</sub>N<sub>4</sub> catalysts with different TiS<sub>2</sub> content were named as x% TiS<sub>2</sub>/2D-C<sub>3</sub>N<sub>4</sub>, where “x” represent the mass percentage of TiS<sub>2</sub> (x = 1, 3, 5, 10 wt%).

### 4. Material characterization

Scanning electron microscope (SEM) images of 5% TiS<sub>2</sub>/2D-C<sub>3</sub>N<sub>4</sub> nanodots were taken on a JEOL-6500 scanning electronic microscope. Transmission electron microscope (TEM) and high resolution TEM (HRTEM) images were recorded on a JEOL-2100F at an accelerating voltage of 200 kV. X-ray diffraction (XRD) patterns of TiS<sub>2</sub> nanodots and the nanocomposites were performed on D/MAX2500V with Cu-Kα radiation (λ = 1.54056 Å). Raman spectra of TiS<sub>2</sub> nanodots, 2D-C<sub>3</sub>N<sub>4</sub> and 5% TiS<sub>2</sub>/2D-C<sub>3</sub>N<sub>4</sub> nanocomposite were acquired with a RENISHAW in Via Raman Microscope using a 532 nm laser excitation. X-ray photoelectron spectroscopy (XPS) measurements were performed to analyze the presence of TiS<sub>2</sub> in the nanocomposites at ambient temperature using PHI Quantera with Al-Kα X-ray source. Shimadzu UV-2450 ultraviolet-visible spectrophotometer was used to collect the UV-vis absorption spectra of TiS<sub>2</sub>/2D-C<sub>3</sub>N<sub>4</sub> nanocomposites. Composition analysis of as-prepared materials was carried on fourier transforms infrared spectrometer (FT-IR) using Nicolet Nexus 470 spectrometer. The ESR spectra were conducted on a Bruker model ESR JES-FA200 spectrometer. Photoluminescence (PL) spectroscopy experiments were conducted at excitation wavelength 377 nm using Jobin Yvon HORIBA NanoLog spectrofluorometer.

### 5. Photocatalytic activity measurements

For photocatalytic degradation experiment, the organic dye RhB was used as a model pollutant. In detail, 10 mg samples were added into 50 ml RhB (10 mg l<sup>−1</sup>) in a Pyrex photocatalytic reactor with a circulating water system to maintain a constant temperature (30 °C). Before irradiation, the suspensions were magnetically stirred for 30 min in the dark to ensure that RhB could reach the absorption–desorption equilibrium on the photocatalyst surface. At a certain time intervals, 3 ml aliquots were sampled and centrifuged to remove the photocatalyst nanoparticles. Then the filtrates were analyzed by recording variations of the absorption band maximum (553 nm) in the UV-vis spectra of RhB using a UV-vis spectrophotometer. The air velocity was 2 l min<sup>−1</sup> and the photocatalytic reaction was performed under a 300 W Xe lamp with a 400 nm cutoff filter.

## Results and discussions

The TiS<sub>2</sub>/2D-C<sub>3</sub>N<sub>4</sub> nanocomposites with different content of TiS<sub>2</sub> nanodots were prepared by solvothermal method in benzyl alcohol. The morphology of 2D-C<sub>3</sub>N<sub>4</sub>, TiS<sub>2</sub> nanodots and the as-prepared 5% TiS<sub>2</sub>/2D-C<sub>3</sub>N<sub>4</sub> nanocomposite were examined by AFM and TEM, as shown in Fig. 1. 2D-C<sub>3</sub>N<sub>4</sub> nanosheets performed a micrometer-scale lateral size and thin thickness about 1–2 nm (Fig. 1a). The size and thickness of TiS<sub>2</sub> nanodots were nanometer grade, 5–10 nm and 1–3 nm (Fig. 1b and c), respectively. Ultrathin and small TiS<sub>2</sub> nanodots were uniformly anchored on the surface of thin 2D-C<sub>3</sub>N<sub>4</sub> nanosheets without hard aggregations. From the HRTEM image, the lattice with spacing of 0.29 nm of TiS<sub>2</sub> nanodots assigned to the (010) planes could be seen on the surface of 2D-C<sub>3</sub>N<sub>4</sub> nanosheets clearly. It demonstrated that the hybridization of 2D-C<sub>3</sub>N<sub>4</sub>



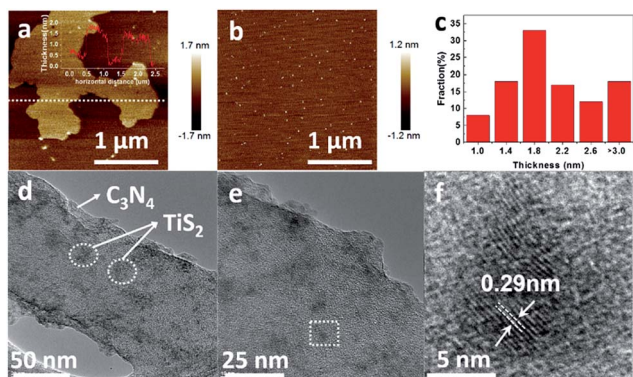


Fig. 1 (a) AFM image and thickness (inset) of 2D-C<sub>3</sub>N<sub>4</sub>; (b) AFM image of TiS<sub>2</sub> nanodots; (c) the statistics of thickness of TiS<sub>2</sub> nanodots; (d) and (e) TEM images and (f) HRTEM image of 5% TiS<sub>2</sub>/2D-C<sub>3</sub>N<sub>4</sub> composite.

nanosheets and TiS<sub>2</sub> nanodots did not disturb the crystal structure and morphology of TiS<sub>2</sub>.

The crystalline structure of the as-prepared TiS<sub>2</sub>/2D-C<sub>3</sub>N<sub>4</sub> nanocomposites with different content of TiS<sub>2</sub> nanodots were further characterized by XRD. In addition to the diffraction peaks at 12.5 and 27.7° attributed to the (100) and (002) crystal planes of 2D-C<sub>3</sub>N<sub>4</sub>, respectively,<sup>44,45</sup> many other peaks for intralayer crystal planes at 15.5, 34.2, 44.2, 53.9, 57.7 and 65.4° of TiS<sub>2</sub>/2D-C<sub>3</sub>N<sub>4</sub> nanocomposites were consistent with those of pure few layers of 1T-TiS<sub>2</sub>.<sup>46</sup> Raman spectra of 5% TiS<sub>2</sub>/2D-C<sub>3</sub>N<sub>4</sub> nanocomposite, 2D-C<sub>3</sub>N<sub>4</sub> and TiS<sub>2</sub> nanodots was taken to further demonstrate the presence of TiS<sub>2</sub> in the nanocomposites (Fig. 2c). The pure TiS<sub>2</sub> nanodots showed a peak at 227 cm<sup>-1</sup> assigned to E<sub>g</sub> and a peak at 332 cm<sup>-1</sup> with a shoulder at 380 cm<sup>-1</sup> attributed to A<sub>1g</sub> vibrational modes of 1T-TiS<sub>2</sub>.<sup>47</sup> However, except for the significant peaks of 2D-C<sub>3</sub>N<sub>4</sub>, the peaks of TiS<sub>2</sub> were not very clear in 5% TiS<sub>2</sub>/2D-C<sub>3</sub>N<sub>4</sub> because of the low content of TiS<sub>2</sub> in the nanocomposites, which was in agreement with previous publications.<sup>48</sup> FT-IR spectra of pure 2D-C<sub>3</sub>N<sub>4</sub> and TiS<sub>2</sub>/2D-C<sub>3</sub>N<sub>4</sub> nanocomposites were obtained as well. Because of the low detective sensitivity and low content of TiS<sub>2</sub> in the nanocomposites, FT-IR spectra of all hybrid only showed typical stretching mode of 2D-C<sub>3</sub>N<sub>4</sub> heterocycles from 1250 to 1700 cm<sup>-1</sup> and the vibrational mode of N-H bond at 3147 cm<sup>-1</sup> respectively.<sup>48</sup>

The chemical states and elemental compositions of TiS<sub>2</sub> nanodots, 2D-C<sub>3</sub>N<sub>4</sub> and 5% TiS<sub>2</sub>/2D-C<sub>3</sub>N<sub>4</sub> nanocomposites were further examined by XPS, as shown in Fig. 3. The C 1s spectra of

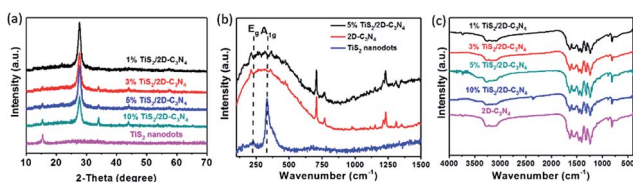


Fig. 2 (a) XRD patterns of TiS<sub>2</sub> nanodots and TiS<sub>2</sub>/2D-C<sub>3</sub>N<sub>4</sub> nanocomposites with different content of TiS<sub>2</sub>; (b) Raman spectra of 2D-C<sub>3</sub>N<sub>4</sub>, TiS<sub>2</sub> nanodots and 5% TiS<sub>2</sub>/2D-C<sub>3</sub>N<sub>4</sub> nanocomposite; (c) FTIR of 2D-C<sub>3</sub>N<sub>4</sub> and TiS<sub>2</sub>/2D-C<sub>3</sub>N<sub>4</sub> nanocomposites.

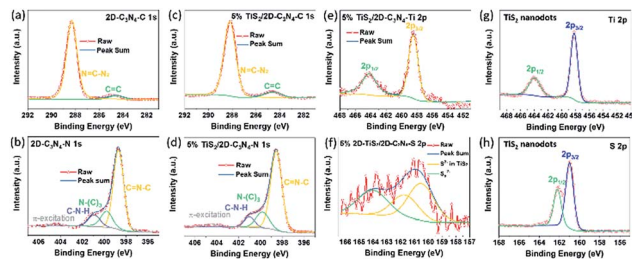


Fig. 3 XPS spectra of 2D-C<sub>3</sub>N<sub>4</sub> and 5% TiS<sub>2</sub>/2D-C<sub>3</sub>N<sub>4</sub> nanocomposites. C 1s (a) and N 1s (b) of 2D-C<sub>3</sub>N<sub>4</sub>; C 1s (c), N 1s (d), Ti 2p (e) and S 2p (f) of 5% TiS<sub>2</sub>/2D-C<sub>3</sub>N<sub>4</sub> nanocomposite; (g) Ti 2p<sub>3/2</sub>, 2p<sub>1/2</sub> and (h) S 2p<sub>3/2</sub>, 2p<sub>1/2</sub> of TiS<sub>2</sub> QDs.

both 2D-C<sub>3</sub>N<sub>4</sub> and 5% TiS<sub>2</sub>/2D-C<sub>3</sub>N<sub>4</sub> nanocomposites showed two peaks at 284.7 eV and 288.2 eV assigned to the sp<sup>2</sup> C=C bonds and N=C-N<sub>2</sub> bonds, respectively (Fig. 3a and c). The N 1s spectrum of 5% TiS<sub>2</sub>/2D-C<sub>3</sub>N<sub>4</sub> nanocomposite with four peaks in Fig. 3b is similar with that of 2D-C<sub>3</sub>N<sub>4</sub> in Fig. 3d. The peaks at 398.7 eV, 399.8 eV, 401.0 eV and 404.4 eV were ascribed to the sp<sup>2</sup>-hybridized nitrogen atoms in C=N-C, the tertiary nitrogen, the amino functions carrying hydrogen (C-N-H) and  $\pi$ -excitation, respectively.<sup>49</sup> The C 1s and N 1s signals confirmed the presence of 2D-C<sub>3</sub>N<sub>4</sub> in 5% TiS<sub>2</sub>/2D-C<sub>3</sub>N<sub>4</sub> nanocomposite, which is consistent with the results in FT-IR. The binding energies of Ti 2p peaks (458.5 eV for 2p<sub>3/2</sub> and 463.3 eV for 2p<sub>1/2</sub>) and the weak binding energies of S<sup>2-</sup> 2p<sub>3/2</sub> and 2p<sub>1/2</sub> peaks emerging at 161.0 eV and 162.2 eV in 5% TiS<sub>2</sub>/2D-C<sub>3</sub>N<sub>4</sub> nanocomposite were similar with the peaks in TiS<sub>2</sub> nanodots, which agreed well with those of 1T-TiS<sub>2</sub>.<sup>50</sup> It demonstrated the existence of TiS<sub>2</sub> nanodots in 5% TiS<sub>2</sub>/2D-C<sub>3</sub>N<sub>4</sub> composite.

The presence of TiS<sub>2</sub> nanodots in the nanocomposites was further studied by SEM images and corresponding EDS. The micro-morphology and element mapping of 5% TiS<sub>2</sub>/2D-C<sub>3</sub>N<sub>4</sub> nanocomposite were shown in Fig. 4. The 2D nanosheets could be seen clearly in Fig. 4a and d. Because TiS<sub>2</sub> nanodots and 2D-C<sub>3</sub>N<sub>4</sub> nanosheets were self-assembled together, it was difficult to distinguish them from morphology. From the element mapping of 5% TiS<sub>2</sub>/2D-C<sub>3</sub>N<sub>4</sub> nanocomposite, it could be seen

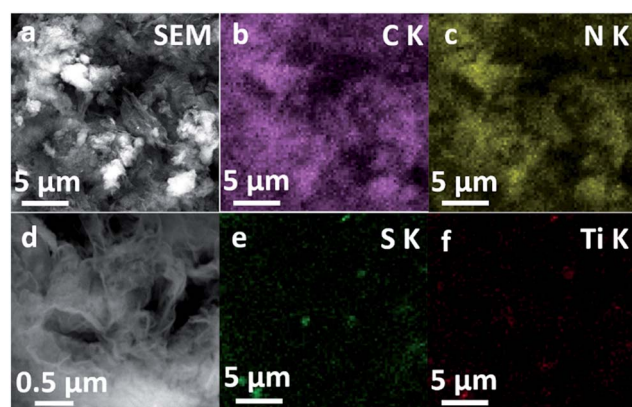


Fig. 4 SEM images and EDX mapping images of 5% TiS<sub>2</sub>/2D-C<sub>3</sub>N<sub>4</sub> nanocomposites. (a) SEM image; EDX mapping of C (b), N (c), S (e), Ti (f); (d) high amplification of SEM image.





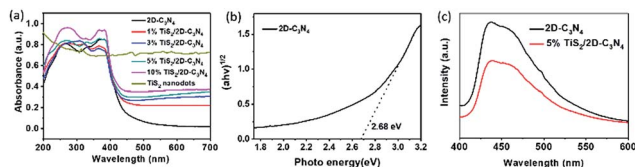


Fig. 5 (a) UV-vis absorption spectra of  $\text{TiS}_2$  nanodots, 2D- $\text{C}_3\text{N}_4$  and  $\text{TiS}_2/2\text{D-C}_3\text{N}_4$  nanocomposites with different content of  $\text{TiS}_2$  nanodots; (b) Tauc plot of pure 2D- $\text{C}_3\text{N}_4$  nanosheets from UV vis absorption. (c) Photoluminescence spectra of pure 2D- $\text{C}_3\text{N}_4$  and 5%  $\text{TiS}_2/2\text{D-C}_3\text{N}_4$  nanocomposite.

that  $\text{TiS}_2$  nanodots were dispersed in the soft nanosheets of 2D- $\text{C}_3\text{N}_4$  uniformly. Ti and S elements of  $\text{TiS}_2$  nanodots were distributed in the matrix C and N elements of 2D- $\text{C}_3\text{N}_4$  in the nanocomposites, which was consistent with the TEM results. As the content of  $\text{TiS}_2$  nanodots in composite was 5%, the signals of Ti and S were much lower than those of C and N.

The UV-vis absorption of pure  $\text{TiS}_2$  nanodots, 2D- $\text{C}_3\text{N}_4$  and as-prepared  $\text{TiS}_2/2\text{D-C}_3\text{N}_4$  nanocomposites were shown in Fig. 5a. The curve of 2D- $\text{C}_3\text{N}_4$  displayed a starting absorption at the edge of visible light blending into the ultraviolet, which corresponded to the band gap of 2D- $\text{C}_3\text{N}_4$  at 2.68 eV in Fig. 5b. And  $\text{TiS}_2$  nanodots could absorb UV and visible light.  $\text{TiS}_2/2\text{D-C}_3\text{N}_4$  nanocomposites performed similar absorption width with 2D- $\text{C}_3\text{N}_4$  nanosheets but much higher absorption value attributed to the light absorption of  $\text{TiS}_2$ , and the absorption intensity at the UV and visible light region were enhanced with increasing content of  $\text{TiS}_2$  nanodots which indicated that  $\text{TiS}_2/2\text{D-C}_3\text{N}_4$  nanocomposites obtained more photogenerated e-h pairs at 200–700 nm. In order to investigate the influence of  $\text{TiS}_2$  QDs on the separation efficiency of the photoexcited carriers in  $\text{TiS}_2/2\text{D-C}_3\text{N}_4$  nanocomposites, the PL spectroscopy measurements were carried out for 2D- $\text{C}_3\text{N}_4$  and 5%  $\text{TiS}_2/2\text{D-C}_3\text{N}_4$  nanocomposites. As shown in Fig. 5c, the fluorescence intensity of emission peak at about 460 nm for 5%  $\text{TiS}_2/2\text{D-C}_3\text{N}_4$  nanocomposite was much weaker than that of 2D- $\text{C}_3\text{N}_4$  due to the low recombination rate of photo-generated charge carriers.<sup>51</sup> Because of the higher UV-vis absorption and lower fluorescence emission intensity, more photo-generated charge carriers in 5%  $\text{TiS}_2/2\text{D-C}_3\text{N}_4$  nanocomposite were trapped by highly conductive  $\text{TiS}_2$  nanodots on 2D- $\text{C}_3\text{N}_4$  nanosheets.

The photocatalytic performance of the nanocomposites was mainly evaluated by photo-degradation of RhB, because RhB is a typical organic dye which is a common water pollutant and could cause long-term environmental toxicity and short-term public health damage. Fig. 6a showed the evolution of the degradation rate of RhB along with time. All the curves had a similar linear downtrend which seemed to be zero-order kinetic process. Hence, the data points were fitted according to the zero-order kinetic process:

$$C/C_0 = -kt + b$$

where  $k$  is the degradation rate constant, and  $b$  represents the residual composition at 0 min. The  $k$ ,  $b$  and  $R^2$  values of the fitted curves for all the samples were listed in Table 1. According to  $R^2$  values of the samples (higher than 0.982), the fitted curves

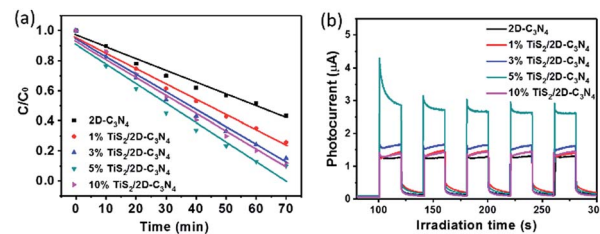


Fig. 6 (a) Photocatalytic activity of RhB in the presence of the 2D- $\text{C}_3\text{N}_4$  and  $\text{TiS}_2/2\text{D-C}_3\text{N}_4$  nanocomposites with different content of  $\text{TiS}_2$  nanodots under visible light. (b) Transient photocurrent response of pure 2D- $\text{C}_3\text{N}_4$  and  $\text{TiS}_2/2\text{D-C}_3\text{N}_4$  nanocomposites.

matched well with the obtained data.<sup>52</sup> So, the degradation behaviour surely followed the zero-order kinetic process. The degradation rate constant of 2D- $\text{C}_3\text{N}_4$  was  $0.00783 \text{ min}^{-1}$ . Compared with blank 2D- $\text{C}_3\text{N}_4$ , all the  $\text{TiS}_2/2\text{D-C}_3\text{N}_4$  nanocomposites exhibited higher photocatalytic degradation rate under the same condition. The addition of  $\text{TiS}_2$  nanodots to 2D- $\text{C}_3\text{N}_4$  enhanced the photocatalytic activity obviously. As the amount of  $\text{TiS}_2$  nanodots increase, the degradation rate of RhB was enhanced significantly. 5%  $\text{TiS}_2/2\text{D-C}_3\text{N}_4$  nanocomposite performed the highest degradation rate among all the catalysts ( $0.0128 \text{ min}^{-1}$ ). When the loading amount of  $\text{TiS}_2$  nanodots reached to 10 wt%, the photocatalytic degradation of RhB decreased as too much  $\text{TiS}_2$  nanodots blocked the photo absorption of 2D- $\text{C}_3\text{N}_4$ . The as-prepared 10%  $\text{TiS}_2/2\text{D-C}_3\text{N}_4$  has higher  $b$  value than 5%  $\text{TiS}_2/2\text{D-C}_3\text{N}_4$  nanocomposite because of weaker absorption ascribed to too high loadings of  $\text{TiS}_2$  nanodots. The highest degradation rate of  $\text{TiS}_2/2\text{D-C}_3\text{N}_4$  nanocomposites was ca. 95% in 70 min, which got an improvement of ca. 30% in comparison with that of 2D- $\text{C}_3\text{N}_4$ . The photocurrent experiment was carried out to explore the charge separation and transfer efficiency (Fig. 6b). The measurements clearly showed that the introduction of  $\text{TiS}_2$  nanodots enhanced the photocurrent of 2D- $\text{C}_3\text{N}_4$ , in which the 5%  $\text{TiS}_2/2\text{D-C}_3\text{N}_4$  nanocomposite exhibited the highest value. The photocurrent for 5%  $\text{TiS}_2/2\text{D-C}_3\text{N}_4$  was about 2.5 times higher than that given by bare 2D- $\text{C}_3\text{N}_4$ . The results above suggested that the introduction  $\text{TiS}_2$  nanodots enhanced the charge separation greatly and suppressed the recombination of e-h pairs, thus an improving the photocatalytic performance.

Besides the high photocatalytic degradation efficiency, the 5%  $\text{TiS}_2/2\text{D-C}_3\text{N}_4$  nanocomposite showed high stability after five times of cyclic experiments (Fig. 7a). In addition, the nanocomposite still preserved the chemical structure of 2D-

Table 1 The  $k$ ,  $b$  and  $R^2$  value following zero-order kinetic process of catalytic degradation

Sample	$b$	$k \text{ (min}^{-1}\text{)}$	$R^2$
2D $\text{C}_3\text{N}_4$	0.96	0.00783	0.982
1% $\text{TiS}_2/2\text{D-C}_3\text{N}_4$	0.97	0.0105	0.992
3% $\text{TiS}_2/2\text{D-C}_3\text{N}_4$	0.94	0.0120	0.985
5% $\text{TiS}_2/2\text{D-C}_3\text{N}_4$	0.90	0.0128	0.990
10% $\text{TiS}_2/2\text{D-C}_3\text{N}_4$	0.97	0.0125	0.986



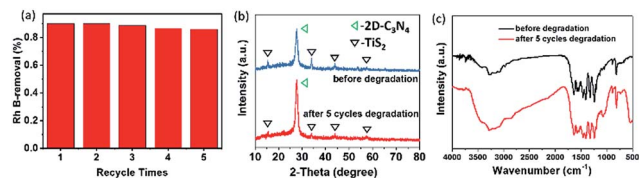


Fig. 7 (a) Cycling runs for the photodegradation of RhB in the presence of 5%  $\text{TiS}_2/2\text{D-C}_3\text{N}_4$  nanocomposite. The chemical and crystal structure of 5%  $\text{TiS}_2/2\text{D-C}_3\text{N}_4$  nanocomposite before and after 5 cycles photodegradation of RhB, XRD pattern (b) and FT-IR spectra (c).

$\text{C}_3\text{N}_4$  and  $\text{TiS}_2$  after five cycles degradation shown by the XRD and FTIR spectra in Fig. 7b and c. The diffraction peak at  $27.7^\circ$  for the (002) crystal plane of  $2\text{D-C}_3\text{N}_4$  and many other peaks at  $15.5$ ,  $34.2$ ,  $44.2$  and  $57.7^\circ$  for intralayer crystal planes of  $\text{TiS}_2$  were consistent with nanocomposite before cycling. FT-IR spectra of  $\text{TiS}_2/2\text{D-C}_3\text{N}_4$  nanocomposites before and after cycling was similar as well.

As discussed above, the metallic  $\text{TiS}_2$  nanodots in the system played a crucial role in the migration of electrons excited by the  $2\text{D-C}_3\text{N}_4$  semiconductor, which could efficiently suppress the recombination of e-h pairs. To gain a further insight into the photocatalytic degradation process, ESR analysis was carried out to explore the active radicals using 5,5-dimethyl-1-pyrroline N-oxide (DMPO) as a spin trapping, as shown in Fig. 8. Obviously, the ESR results showed that, when  $\text{TiS}_2/2\text{D-C}_3\text{N}_4$  nanocomposite were employed as photocatalyst, both  $\text{O}_2^{\cdot-}$  and  $\cdot\text{OH}$  could be generated under visible light irradiation. According to previous reports, the top of valence band (TVB) potential of  $2\text{D-C}_3\text{N}_4$  was  $1.79\text{ V vs. RHE}$ .<sup>53,54</sup> The band gap was calculated to be  $2.68\text{ eV}$  (Fig. 5b), thus the bottom of conduction band (BCB) potential of  $2\text{D-C}_3\text{N}_4$  was  $-0.89\text{ V vs. RHE}$ . Apparently, the potential energy of the photo-excited electrons at BCB potential was higher than that of  $\text{O}_2^{\cdot-}/\text{O}_2$  ( $-0.046\text{ eV}$ ), thus the electrons possessed the ability to combine with  $\text{O}_2$  into  $\text{O}_2^{\cdot-}$ . For the generation of  $\cdot\text{OH}$ , the holes at the TVB of  $2\text{D-C}_3\text{N}_4$  cannot oxidize  $\text{H}_2\text{O}$  or  $\text{OH}^-$  into  $\cdot\text{OH}$  due to the lower TVB position in comparison with  $\text{OH}^-/\cdot\text{OH}$  ( $1.99\text{ eV}$ ) and  $\text{H}_2\text{O}/\cdot\text{OH}$  ( $2.38\text{ eV}$ ). The  $\cdot\text{OH}$  may be generated by the further reactions of strong reduction  $\text{O}_2^{\cdot-}$  through an intermediate of  $\cdot\text{OOH}$ .<sup>55-57</sup>

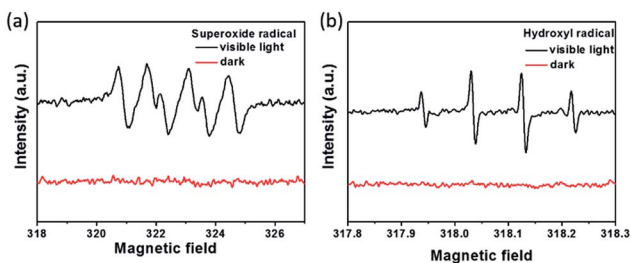


Fig. 8 (a) ESR spectra of  $\text{DMPO-O}_2^{\cdot-}$  (a) and  $\text{DMPO-}\cdot\text{OH}$  (b) adducts in  $\text{TiS}_2/2\text{D-C}_3\text{N}_4$  aqueous dispersion systems under visible light irradiation or in the dark.

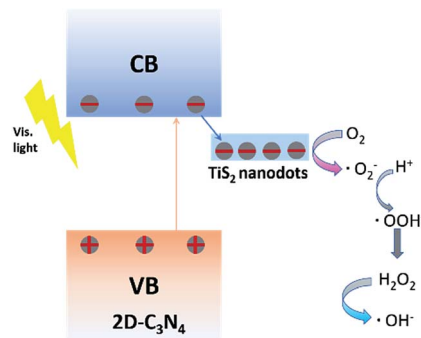


Fig. 9 The degradation of mechanism of as-prepared  $\text{TiS}_2/2\text{D-C}_3\text{N}_4$  composites.

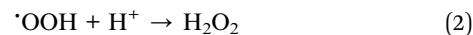


Fig. 9 is a schematic illustration of the synergistic effect of the photocatalytic process. In a typical photocatalytic degradation process, the  $2\text{D-C}_3\text{N}_4$  nanosheets could photogenerated e-h pairs under visible light firstly. Afterwards, the electrons kept at conduction band would be efficiently trapped by metallic  $\text{TiS}_2$  nanodots as co-catalyst. The high concentration of electrons could react with  $\text{O}_2$  to form active radicals  $\text{O}_2^{\cdot-}$ . Due to the strong reduction of the photogenerated electrons, the formed  $\text{O}_2^{\cdot-}$  also possessed very strong reduction which led to the further reactions and formation of  $\cdot\text{OH}$  radicals through an intermediate of  $\cdot\text{OOH}$  as listed from reaction (1) to (3). The radicals  $\text{O}_2^{\cdot-}$  and  $\cdot\text{OH}$  were well known as effective radicals for water pollutant treatment. In addition, the hole at valence band of  $2\text{D-C}_3\text{N}_4$  could oxidize pollutant directly. The metallic nature of  $\text{TiS}_2$  nanodots and the construction of tight interface between the two components were beneficial for the separation and transfer of photo-excited carriers. Therefore, high concentration of photogenerated electrons could converge for photocatalytic reactions at  $\text{TiS}_2$  nanodots instead of recombination at  $2\text{D-C}_3\text{N}_4$  nanosheets.

## Conclusion

We utilized a simple exfoliation synthesis to get ultrathin  $\text{TiS}_2$  nanodots and the  $\text{TiS}_2/2\text{D-C}_3\text{N}_4$  was synthesized by a temperate solvothermal method. The  $\text{TiS}_2$  nanodots were tightly anchored on the surface of  $2\text{D-C}_3\text{N}_4$  nanosheets and the inherent metallic nature of  $1\text{T-TiS}_2$  improved the photocatalytic degradation activity due to the effective suppression of the e-h recombination and the higher light absorption. Noteworthy, the content of the  $\text{TiS}_2$  nanodots in the prepared complex played a role in the RhB photocatalytic degradation. The 5%  $\text{TiS}_2/2\text{D-C}_3\text{N}_4$  exhibited the best photocatalytic performance and the degradation rate towards RhB was *ca.* 95% in 70 min, which got an improvement of *ca.* 30% in comparison with pure  $2\text{D-C}_3\text{N}_4$  nanosheets. So, the combination of ultrathin metallic TMDs with  $2\text{D}$  graphitic  $\text{C}_3\text{N}_4$  yields a promising photocatalyst for practical application.



## Conflicts of interest

There are no conflicts to declare.

## Acknowledgements

This research is financially supported by the National Natural Science Foundation of China (NNSFC Grant No. 51422305, 21476097).

## Notes and references

- 1 S. Cao, J. Low, J. Yu and M. Jaroniec, *Adv. Mater.*, 2015, **27**, 2150–2176.
- 2 H. Xu, L. Liu, X. She, Z. Mo, Y. Xu, L. Huang, Y. Song and H. Li, *RSC Adv.*, 2016, **6**, 80193–80200.
- 3 C. M. Fang, R. A. de Groot and C. Haas, *Phys. Rev. B: Condens. Matter Mater. Phys.*, 1997, **56**, 4455–4463.
- 4 A. Fujishima and K. Honda, *Nature*, 1972, **238**, 37–38.
- 5 M. Zhu, C. Zhai, L. Qiu, C. Lu, A. S. Paton, Y. Du and M. C. Goh, *ACS Sustainable Chem. Eng.*, 2015, **3**, 3123–3129.
- 6 I. Hwang, I. Jeong, J. Lee, M. J. Ko and K. Yong, *ACS Appl. Mater. Interfaces*, 2015, **7**, 17330–17336.
- 7 H. Tong, S. Ouyang, Y. Bi, N. Umezawa, M. Oshikiri and J. Ye, *Adv. Mater.*, 2012, **24**, 229–251.
- 8 J. Li, X. Zhang, F. Raziq, J. Wang, C. Liu, Y. Liu, J. Sun, R. Yan, B. Qu, C. Qin and L. Jing, *Appl. Catal., B*, 2017, **218**, 60–67.
- 9 J. Shen, Y. He, J. Wu, C. Gao, K. Keyshar, X. Zhang, Y. Yang, M. Ye, R. Vajtai, J. Lou and P. M. Ajayan, *Nano Lett.*, 2015, **15**, 5449–5454.
- 10 M. Chhowalla, H. S. Shin, G. Eda, L. J. Li, K. P. Loh and H. Zhang, *Nat. Chem.*, 2013, **5**, 263–275.
- 11 Q. Lu, Y. Yu, Q. Ma, B. Chen and H. Zhang, *Adv. Mater.*, 2016, **28**, 1917–1933.
- 12 Y. Sang, Z. Zhao, M. Zhao, P. Hao, Y. Leng and H. Liu, *Adv. Mater.*, 2015, **27**, 363–369.
- 13 S. Yang, Y. Gong, J. Zhang, L. Zhan, L. Ma, Z. Fang, R. Vajtai, X. Wang and P. M. Ajayan, *Adv. Mater.*, 2013, **25**, 2452–2456.
- 14 Y. Zhou, Y. Zhang, M. Lin, J. Long, Z. Zhang, H. Lin, J. C. Wu and X. Wang, *Nat. Commun.*, 2015, **6**, 8340.
- 15 J. Low, S. Cao, J. Yu and S. Wageh, *Chem. Commun.*, 2014, **50**, 10768–10777.
- 16 P. Yang, H. Ou, Y. Fang and X. Wang, *Angew. Chem.*, 2017, **129**, 4050–4054.
- 17 V. Subramanian, E. E. Wolf and P. V. Kamat, *Langmuir*, 2003, **19**, 469–474.
- 18 K. Awazu, M. Fujimaki, C. Rockstuhl, J. Tominaga, H. Murakami, Y. Ohki, N. Yoshida and T. Watanabe, *J. Am. Chem. Soc.*, 2008, **130**, 1676–1680.
- 19 S. Sakthivel, M. Shankar, M. Palanichamy, B. Arabindoo, D. Bahnemann and V. Murugesan, *Water Res.*, 2004, **38**, 3001–3008.
- 20 C. Han, Y. Lu, J. Zhang, L. Ge, Y. Li, C. Chen, Y. Xin, L. Wu and S. Fang, *J. Mater. Chem. A*, 2015, **3**, 23274–23282.
- 21 R.-B. Wei, P.-Y. Kuang, H. Cheng, Y.-B. Chen, J.-Y. Long, M.-Y. Zhang and Z.-Q. Liu, *ACS Sustainable Chem. Eng.*, 2017, **5**, 4249–4257.
- 22 M. Sun, J. Hu, C. Zhai, M. Zhu and J. Pan, *ACS Appl. Mater. Interfaces*, 2017, **9**, 13223–13230.
- 23 X. Pan and Y.-J. Xu, *J. Phys. Chem. C*, 2013, **117**, 17996–18005.
- 24 V. Nicolosi, M. Chhowalla, M. G. Kanatzidis, M. S. Strano and J. N. Coleman, *Science*, 2013, **340**, 1226419.
- 25 X. Huang, C. Tan, Z. Yin and H. Zhang, *Adv. Mater.*, 2014, **26**, 2185–2204.
- 26 H. Li, J. Wu, Z. Yin and H. Zhang, *Acc. Chem. Res.*, 2014, **47**, 1067–1075.
- 27 Z. Zeng, C. Tan, X. Huang, S. Bao and H. Zhang, *Energy Environ. Sci.*, 2014, **7**, 797–803.
- 28 C. Tan, Z. Zeng, X. Huang, X. Rui, X. J. Wu, B. Li, Z. Luo, J. Chen, B. Chen, Q. Yan and H. Zhang, *Angew. Chem., Int. Ed.*, 2015, **54**, 1841–1845.
- 29 P.-Y. Kuang, Y.-Z. Su, K. Xiao, Z.-Q. Liu, N. Li, H.-J. Wang and J. Zhang, *ACS Appl. Mater. Interfaces*, 2015, **7**, 16387–16394.
- 30 D. Chu, C. Zhang, P. Yang, Y. Du and C. Lu, *Catalysts*, 2016, **6**, 136.
- 31 J. Chen, S. L. Li and Z. L. Tao, *J. Am. Chem. Soc.*, 2003, **125**, 5284–5285.
- 32 G. Guelou, P. Vaqueiro, J. Prado-Gonjal, T. Barbier, S. Hebert, E. Guilmeau, W. Kockelmann and A. V. Powell, *J. Mater. Chem. C*, 2016, **4**, 1871–1880.
- 33 U. Gupta, B. G. Rao, U. Maitra, B. E. Prasad and C. N. Rao, *Chem.-Asian J.*, 2014, **9**, 1311–1315.
- 34 W. Cui, J. Li, W. Cen, Y. Sun, S. C. Lee and F. Dong, *J. Catal.*, 2017, **352**, 351–360.
- 35 X. She, L. Liu, H. Ji, Z. Mo, Y. Li, L. Huang, D. Du, H. Xu and H. Li, *Appl. Catal., B*, 2016, **187**, 144–153.
- 36 X. She, H. Xu, Y. Xu, J. Yan, J. Xia, L. Xu, Y. Song, Y. Jiang, Q. Zhang and H. Li, *J. Mater. Chem. A*, 2014, **2**, 2563.
- 37 X. She, H. Xu, H. Wang, J. Xia, Y. Song, J. Yan, Y. Xu, Q. Zhang, D. Du and H. Li, *Dalton Trans.*, 2015, **44**, 7021–7031.
- 38 Q. Han, B. Wang, J. Gao, Z. Cheng, Y. Zhao, Z. Zhang and L. Qu, *ACS Nano*, 2016, **10**, 2745–2751.
- 39 H. Wang, Y. Su, H. Zhao, H. Yu, S. Chen, Y. Zhang and X. Quan, *Environ. Sci. Technol.*, 2014, **48**, 11984–11990.
- 40 G. Zhang, Z. A. Lan and X. Wang, *Angew. Chem., Int. Ed.*, 2016, **55**, 15712–15727.
- 41 Y. Cui, Y. Tang and X. Wang, *Mater. Lett.*, 2015, **161**, 197–200.
- 42 M. Zhu, C. Zhai, M. Sun, Y. Hu, B. Yan and Y. Du, *Appl. Catal., B*, 2017, **203**, 108–115.
- 43 Y. Wang, H. Wang, F. Chen, F. Cao, X. Zhao, S. Meng and Y. Cui, *Appl. Catal., B*, 2017, **206**, 417–425.
- 44 Y. Shang, X. Chen, W. Liu, P. Tan, H. Chen, L. Wu, C. Ma, X. Xiong and J. Pan, *Appl. Catal., B*, 2017, **204**, 78–88.
- 45 T. Y. Ma, Y. Tang, S. Dai and S. Z. Qiao, *Small*, 2014, **10**, 2382–2389.
- 46 S. Jeong, D. Yoo, M. Ahn, P. Miró, T. Heine and J. Cheon, *Nat. Commun.*, 2015, **6**, 5763.
- 47 S. J. Sandoval, X. K. Chen and J. C. Irwin, *Phys. Rev. B: Condens. Matter Mater. Phys.*, 1992, **45**, 14347–14353.
- 48 X. Lu, Y. Jin, X. Zhang, G. Xu, D. Wang, J. Lv, Z. Zheng and Y. Wu, *Dalton Trans.*, 2016, **45**, 15406–15414.
- 49 J. Liu, H. Xu, Y. Xu, Y. Song, J. Lian, Y. Zhao, L. Wang, L. Huang, H. Ji and H. Li, *Appl. Catal., B*, 2017, **207**, 429–437.



- 50 R. J. Toh, Z. Sofer and M. Pumera, *J. Mater. Chem. A*, 2016, **4**, 18322–18334.
- 51 G. Dong, Y. Zhang, Q. Pan and J. Qiu, *J. Photochem. Photobiol., C*, 2014, **20**, 33–50.
- 52 X. Liu, N. Chen, Y. Li, D. Deng, X. Xing and Y. Wang, *Sci. Rep.*, 2016, **6**, 39531.
- 53 X. She, J. Wu, H. Xu, J. Zhong, Y. Wang, Y. Song, K. Nie, Y. Liu, Y. Yang, M.-T. F. Rodrigues, R. Vajtai, J. Lou, D. Du, H. Li and P. M. Ajayan, *Adv. Energy Mater.*, 2017, **7**, 1700025.
- 54 J. Yi, X. She, Y. Song, H. Xu, P. Zhang, Z. Mo, L. Liu, D. Du and H. Li, *RSC Adv.*, 2016, **6**, 112420–112428.
- 55 M. R. Hoffmann, S. T. Martin, W. Choi and D. W. Bahnemann, *Chem. Rev.*, 1995, **95**, 69–96.
- 56 S. Yan, Z. Li and Z. Zou, *Langmuir*, 2010, **26**, 3894–3901.
- 57 Y. Cui, J. Huang, X. Fu and X. Wang, *Catal. Sci. Technol.*, 2012, **2**, 1396–1402.

